Supporting Information for:

Chamber studies of OH + dimethyl sulfoxide and dimethyl disulfide: insights into the dimethyl sulfide oxidation mechanism

S.1 Detailed quantification methods for gas-phase species

S.1.1 DMDS

DMDS was quantified using a gas-chromatography-flame-ionization-detector (SRI GC-FID). For each run, air was pulled through a trap (Supelco 2-0370-U) at 0.5 LPM, then heated and flushed onto the column. The full GC method is shown in Table S1.

Table S1: GC-FID operation details showing time, events, and the oven temperature program.

Time (minutes)	Event	Temperature program
0.0	Zero the signal	Hold 50° C for 5 min
0.1	Pump turned on to sample air through trap	
3.0	Pump turned off	
3.1	Trap heater turned on (setpoint = 300 °C)	
4.1	Helium flushed through trap onto column	
5.0		Ramp at 100° C / min to 140° C
5.9		Ramp at 40° C / min to 220° C
7.0	Trap heater turned off	
7.9		Hold at 220° C for 1.1 minutes
8.9	Valves reset to sample position	
9.0	End signal recording	Oven cooling
13.75	Next sample started	

DMDS eluted as a well-defined peak at t = 420-435 seconds. Dichloromethane used to wash the $NaNO_3$ seed particle solution was also detected as a broad peak (t = 350-510 seconds). To separate these, a spline fit to the dichloromethane peak was subtracted from the total signal to yield a clean DMDS signal. The sensitivity of the instrument to DMDS was 8.2 mV s ppb^{-1} based on three independent chamber injections of known volumes and remained stable across experiments performed two months apart.

Due to the long gaps between each measurement timepoint and the short duration of experiment 6, the point at t = 0 for this experiment is extrapolated based on the three points before t = 0 (See Fig. S11b).

S.1.2 Gas-phase organic species

Gas-phase organic species were measured using the NH_4^+-CIMS sampling directly from the chamber (DMDS experiments), or with a mass flow controller supplying clean air to dilute the sample flow by a factor of ~14 (DMSO experiments) to avoid overwhelming the primary ion with the DMSO signal. The dilution factor was quantified by adding acetonitrile to the chamber before the dilution was started; when the dilution flow was started, the reduction in the acetonitrile signal provides a precise measurement of the dilution factor. During experiment 3, the mass flow controller reset to zero, stopping the dilution flow, and overwhelming the primary ion with DMSO. NH_4^+-CIMS data from this experiment are therefore reported with a gap in the timeseries. To facilitate quantification, collision-induced dissociation (CID) scans (Zaytsev et al., 2019) were run during each experiment; timeseries data shown in plots are interpolated across these short gaps.

Raw NH_4^+-CIMS data were processed in PTRwid (Holzinger, 2015). Product ions, detected as mass + NH_4^+, were separated from background ion signals using hierarchical clustering based on their normalized timeseries (Koss et al., 2020). Where analytical standards were not available, instrument sensitivity for each ion was estimated by comparing CID scans to CID scans carried out on a mixture of VOCs of known concentrations (See Zaytsev et al. (2019)). Instrument signal was divided by the sensitivity to obtain concentrations. Calculated sensitivities remained relatively stable between experiments. Compounds for which the signal was too low to show clear response to the CID scan, and compounds whose molecular formula did not represent a closed-shell species were removed.

DMSO was calibrated directly using a liquid calibration unit (Ionicon Analytik). A solution of DMSO (10 µL DMSO in 20 mL MilliQ water) was atomized and vaporized into the NH_4^+-CIMS inlet, and the liquid flow rate was adjusted to provide a multipoint calibration. This was also attempted for MSIA using acidified sodium methanesulfinate but was not successful.

S.1.3 SO₂ and NOₓ

SO_2 and NO_X monitors were calibrated using analytical standard gas cylinders. The NO_X monitor measures NO, total NO_X, and by subtraction, NO_2. For the total NO_X channel, NO_2 and other NO_Y species are catalytically converted to NO, such that NO_2 and HONO are indistinguishable. Assuming unit conversion of NO_Y species, the NO_2 channel therefore represents $NO_2 + NO_Y$. For experiments where HONO is added, the entirety of the NO_2 signal at the beginning of the experiment is assumed to be HONO (Table 1) though this represents an upper bound. Substantial NO is also observed to form when HONO is generated (see Fig. S4 and S5).

S.1.4 Data synthesis

All gas-phase species were corrected for dilution loss by dividing by a normalized exponential fit of the acetonitrile timeseries. This fit is derived from t = 0 to the end of the experiment, except for experiment 5, for which the fit is carried from t = 1500 s to the end of the experiment due to a

deviation in the acetonitrile timeseries. Gas-phase and particle-phase data are combined into one dataset, background subtracted, and block averaged on 180 second intervals for most plots.

S.2 Detailed AMS quantification methods

Quantification of particle-phase products using the AMS followed a new method developed to measure the concentration of MSIA and MSA. Prior to the experiments, the AMS relative ionization efficiency (RIE) for MSA was calibrated following the method of Hodshire et al. (2019). Methanesulfonic acid (Signa Aldrich, > 99.0%) was reacted with excess ammonium hydroxide (VWR, 28-30%) to form a solution of ammonium methanesulfonate (NH_4MSA). Reference spectra were also taken for ammonium sulfate (Sigma Aldrich, >99.0%), ammonium methanesulfonate, and sodium methanesulfinate (NaMSIA) (Sigma Aldrich, 85%) by atomizing these compounds into the AMS. These spectra are processed as described below and shown in Fig. S1.

To process experimental data, raw AMS data is first processed in Igor. AMS data were processed in SQUIRREL 1.63B and PIKA 1.23B to obtain high resolution product spectra. These data are grouped by chemical family and exported as matrices of spectra over time. This is done for HRSO4, HRNO3, familyCS, familyOther, familyCH, familyCHO1, familyCHOgt1, and familyCx.

Next, the exported data are processed in R to reshape the data structure. The exported matrices are first recalculated to be timeseries over each unit-mass-resolution m/z value instead of each HR ion. Only peaks below *m/z* 115 are used due to uncertainty in fit for higher masses. Timeseries corresponding to HS^+, H_2S^+, H_3S^+, and their isotopes are taken from familyOther and added to familyCS. All C-containing families (CH, CHO1, CHOgt1, and Cx) are summed together to make a new familyC. Note that "HR aerosol species" have the HR Frag Table applied, which corrects for specific overlapping peaks, but "HR families" do not. This matters most notably for S^+ which overlaps with the O_2^+ signal. Using "HRSO4" (the aerosol species) corrects for this issue. Therefore, the new familyCS, familyC, and HRSO4 data are saved for further analysis. This process of restructuring HR output data is also done for the reference spectra. However, for the reference spectra, any non-sulfur-containing organic peak with a mass greater than CH_4O^+ is set to zero to avoid including any background ions in the reference. These reference spectra are shown in Fig. S1.

The reference spectra demonstrate the differences between MSA and MSIA as they appear in the AMS. While they share similar dominant peaks, the MSA spectrum features notable familyCS peaks at masses 78 ($CH_2SO_2^+$), 79 ($CH_3SO_2^+$), and 96 ($CH_4SO_3^+$). The distribution of familyCS peaks with masses below m/z 63 is also different. While MSA is usually quantified based on the m/z 79 peak (Hodshire et al., 2019), we observe a small signal from MSIA at the same mass, suggesting that this cannot uniquely separate them. We therefore rely on a linear combination of the MSA and MSIA spectra to derive their respective components from the product spectra. We note that we observe a peak at m/z 125 in the MSIA reference spectrum that is not able to be identified with this mass spectral resolution. This may be due to an impurity in the technical

grade NaMSIA standard and due to the uncertainty in its identification, it is left out of further analysis.
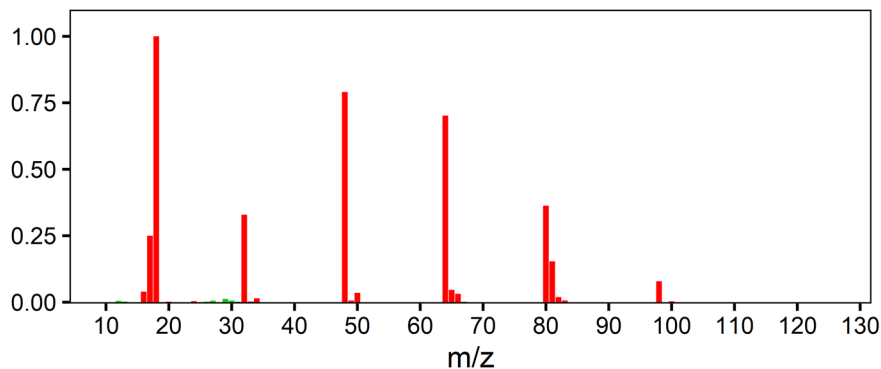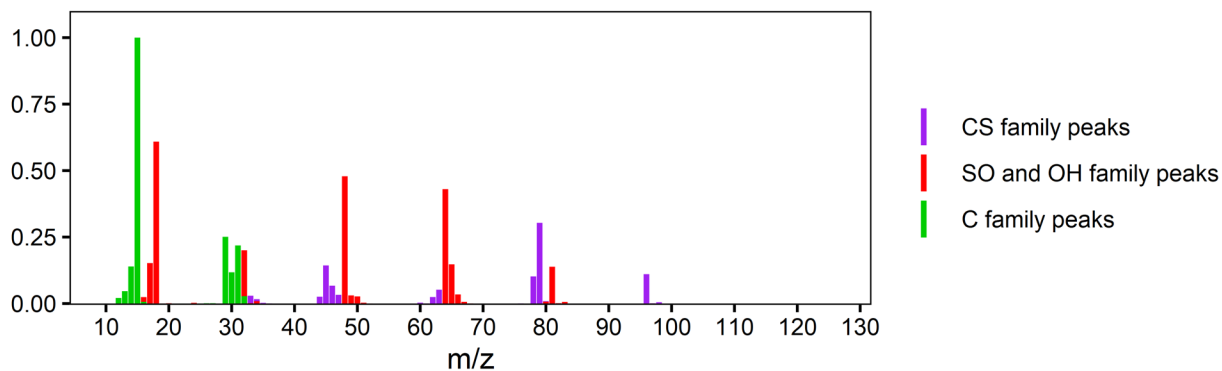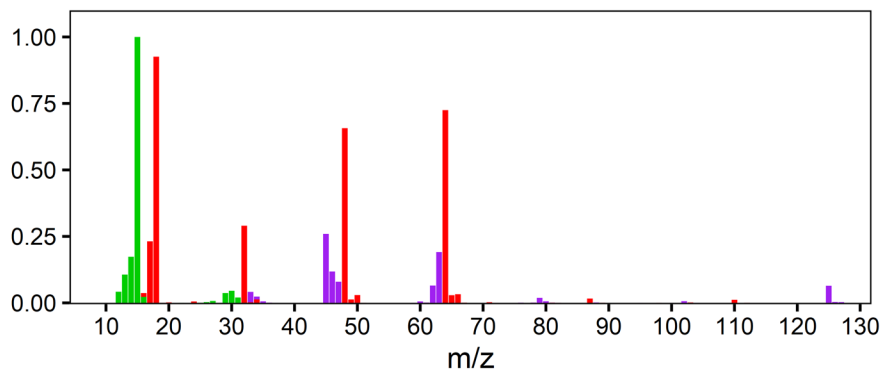
Figure S1: Reference spectra for ammonium sulfate (Panel a), ammonium methanesulfonate (Panel b), and sodium methanesulfinate (Panel c). These spectra leave out the ammonium peaks for simplicity and focus only on the chemical families used in this analysis. Chemical families are grouped as described in the text. "SO and OH family peaks" refers to the "HRSO4" family generated in PIKA.

Following this reclassification of some species, the data are fit as a linear combination of reference spectra to derive MSIA and MSA factors. Since the most unique features of the mass spectra for MSA and MSIA are peaks containing C, H, and S, only familyCS peaks are used for the linear fit. At each timepoint, the familyCS spectrum from the experimental AMS data is fit as a linear combination of the familyCS spectra from the MSA and MSIA reference data with 0 set as the intercept. These fit coefficients are then applied to the full reference MSA and MSIA spectra, and the peaks are summed to generate a timeseries of MSA and MSIA. The r^2 value from the linear combination was typically around 0.95 in these experiments. An example timeseries of the MSA and MSIA coefficients from the regression and the r^2 value are shown in Fig. S2.
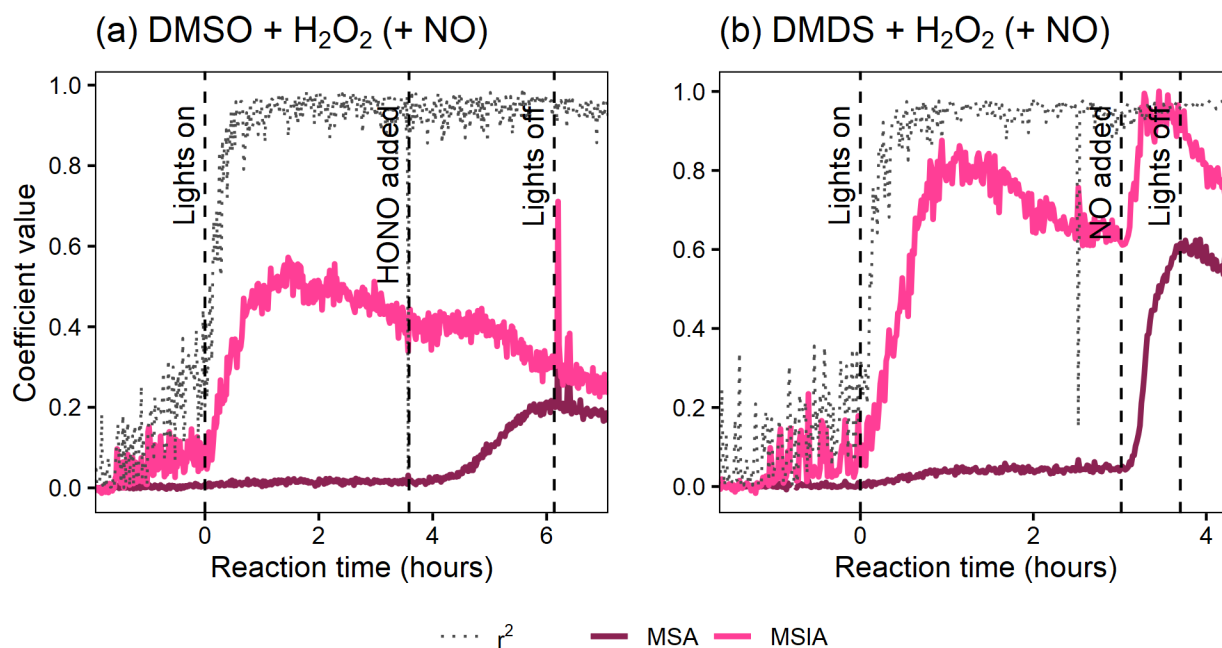
Figure S2: Example timeseries of the MSA and MSIA coefficients from the linear combination fits of familyCS peaks, in addition to the r^2 values over time. Panel a shows the fit from experiment 1 in which DMSO was oxidized (median r^2 = 0.95). Panel b shows the fit from experiment 5 in which DMDS was oxidized (median r^2 = 0.96).

To generate a sulfate timeseries, the "HRSO4" peaks from the derived MSA and MSIA spectral timeseries are subtracted from the original HRSO4 spectra over time. This gives a residual sulfate spectrum over time. The peaks are summed to generate a sulfate timeseries. We note that the distribution of sulfate peaks is not constant over time and appears to be influenced by the sodium counterion. $NaSO_3^+$ is first seen in much greater abundance than SO_3^+ but these ions swap in relative abundance as the experiment proceeds. This is likely due to loss of $NaNO_3$ seed particles to the walls and dilution while sulfate continues to be produced through gas-phase chemistry. An example of this change over time is shown in Fig. S3.
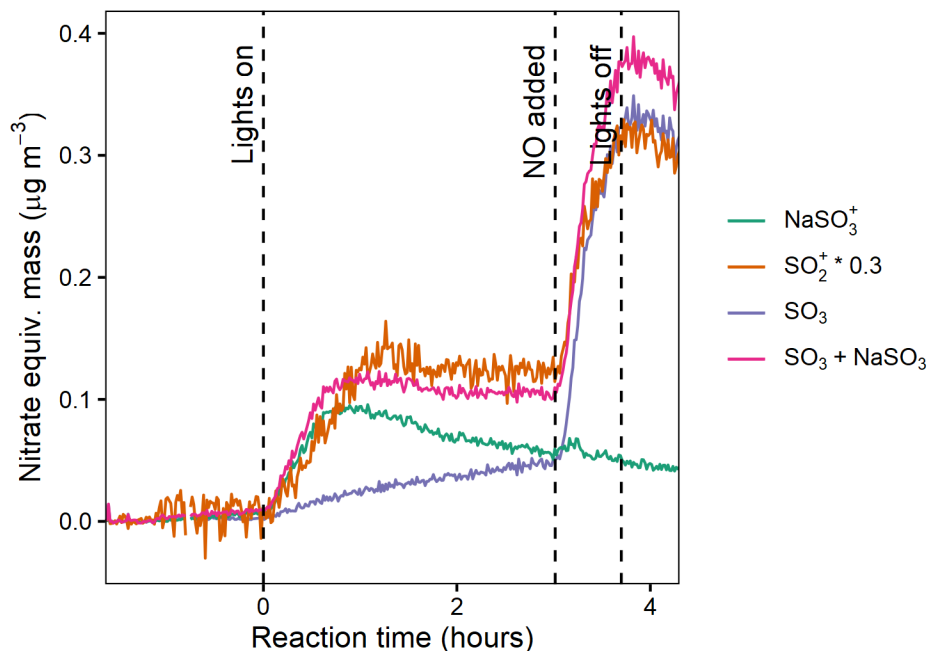
Figure S3: Timeseries of selected AMS ions from experiment 5 (DMDS). The spectrum of the sulfate residual shifts over time, most dramatically between the SO_3^+ and the $NaSO_3^+$ peaks. As sulfate is produced throughout the experiment, sulfuric acid becomes the more dominant form, shifting SO_3 away from the Na^+ counterion. Summing the SO_3^+ and $NaSO_3^+$ signal gives a timeseries that is relatively consistent with the SO_2^+ signal, suggesting that this is merely a change in counterion rather than a different sulfate species. After these ions are summed, the full spectrum is relatively constant over the length of the experiment.

The same subtraction approach is used to generate an organic residual timeseries. This is small (generally 1-2 µg m^{-3} before dilution and wall loss correction) and is introduced as an organic contaminant on the seed aerosol particles. It generally decreases with the seed aerosol signal though in some cases increases slightly towards the end of experiments. Since it does not contain sulfur, it is not considered further in this analysis.

Since the derived timeseries are in nitrate equivalent mass, appropriate RIE values are applied to each species. We measured RIE for MSA to be 2.06 using the ammonium balance method (Hodshire et al., 2019). Since we do not have ammonium methanesulfinate (NH$_4$MSIA), this method cannot be used for MSIA and we therefore assume the same RIE value for MSIA. Data are wall loss and dilution corrected by dividing by the normalized HRNO3 timeseries, and collection efficiency is corrected for by comparing the mass of the seed particles measured by the AMS to SMPS data. The timeseries are finally converted to ppbS based on literature molecular weights and densities for MSA and MSIA.

We note that deconvolving AMS spectra involves inherent uncertainty due to the nature of fragmentation observed (for example, organic species are typically assigned to a general "Org" signal due to the number and complexity of common peaks). For systems such as DMSO oxidation where MSA and MSIA are the only likely organosulfur species that can contribute to the aerosol, this decomposition appears to work well. As noted in the main text, DMDS

oxidation generates additional organosulfur species which may condense onto the aerosol particles. If found in the aerosol phase, these may fragment to form similar distributions of common organosulfur ions (e.g. CHS^+, CH_2S^+ etc.). While the decomposition between MSA and MSIA fractions represents a reasonable best estimate based on expected products and the reference standards available and consistently fits the data well (see Fig. S2b), it may not describe the actual species present in the aerosol, particularly for complex organosulfur oxidation systems. The discrepancy in apparent gas-aerosol partitioning for MSIA in DMSO vs DMDS data is described in the main text, and used to conclude that the MSIA fraction for DMDS may consist of additional organosulfur species. This method should therefore be used to analyze data for which both MSA and MSIA are expected to be present and should be accorded appropriate uncertainty where other organosulfur species may significantly contribute to the aerosol.

S.3 NO_X and Ozone data
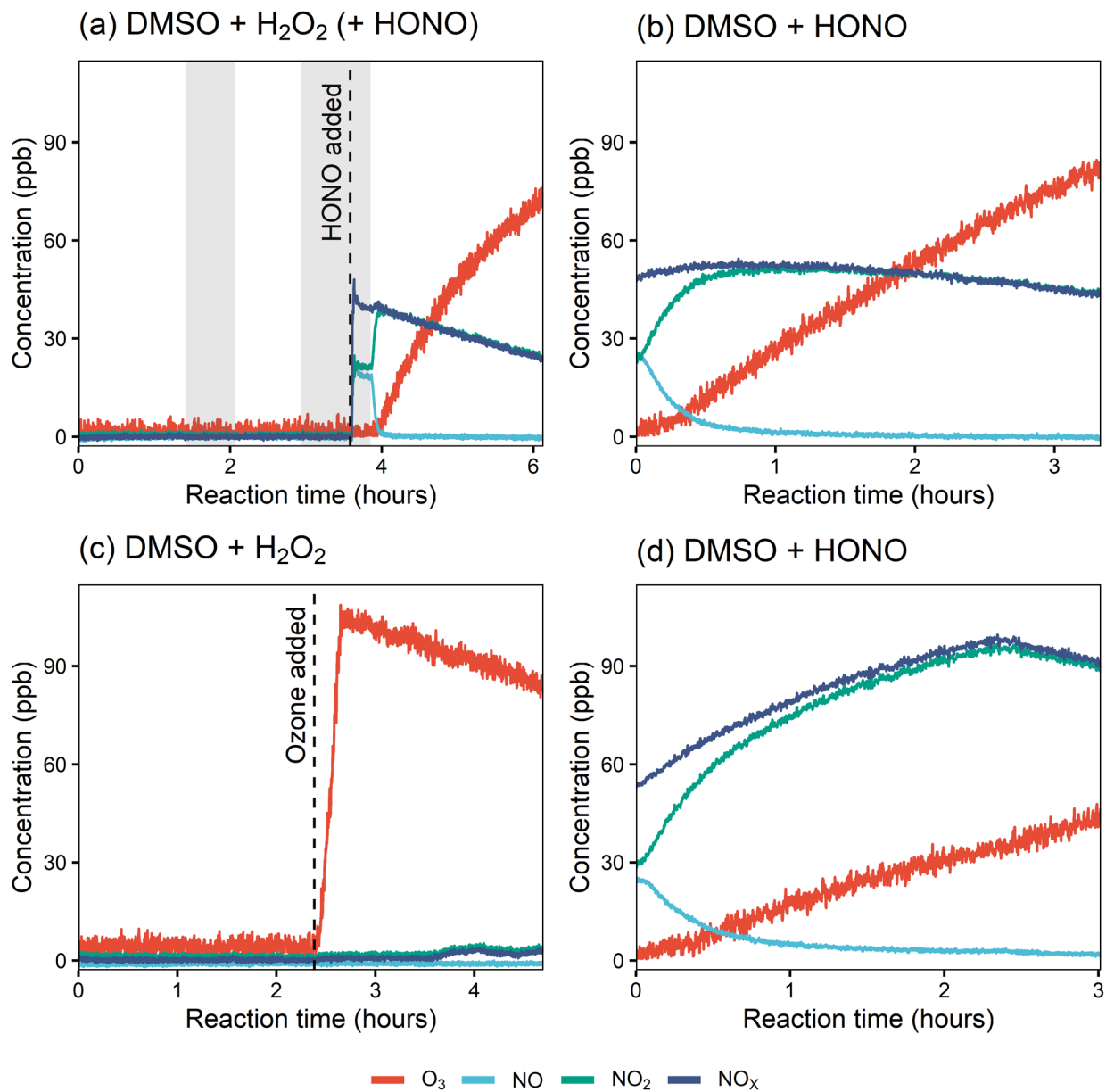
Figure S4: NO_X and ozone timeseries from DMSO oxidation experiments (Panels a-d correspond to experiments 1-4 respectively). Note that NO_Y species such as HONO are measured as NO₂ in the NO_X monitor so "NO₂" represents NO₂ + NO_Y. No dilution corrections have been applied to these data. Note that the x-axes are different in each panel. The gray bars represent times when the lights were turned off for diagnostic purposes.

Figure S4 shows NO_X and ozone timeseries from experiments in which DMSO was oxidized. As described briefly in the main text, HONO (detected as NO_2) is formed with considerable NO as a byproduct (Panels a, b, d). Total NO_X is observed to rise in Panels b and d; this is due to passive diffusion of HONO from the headspace of the H_2SO_4 and $NaNO_2$ solution through an open line to the chamber. In experiment 4, this line was left open until it was fully disconnected at $t = 2.37$ hours. The HONO solution was also left connected to the chamber for experiment 2 but appears to have diffused more slowly.
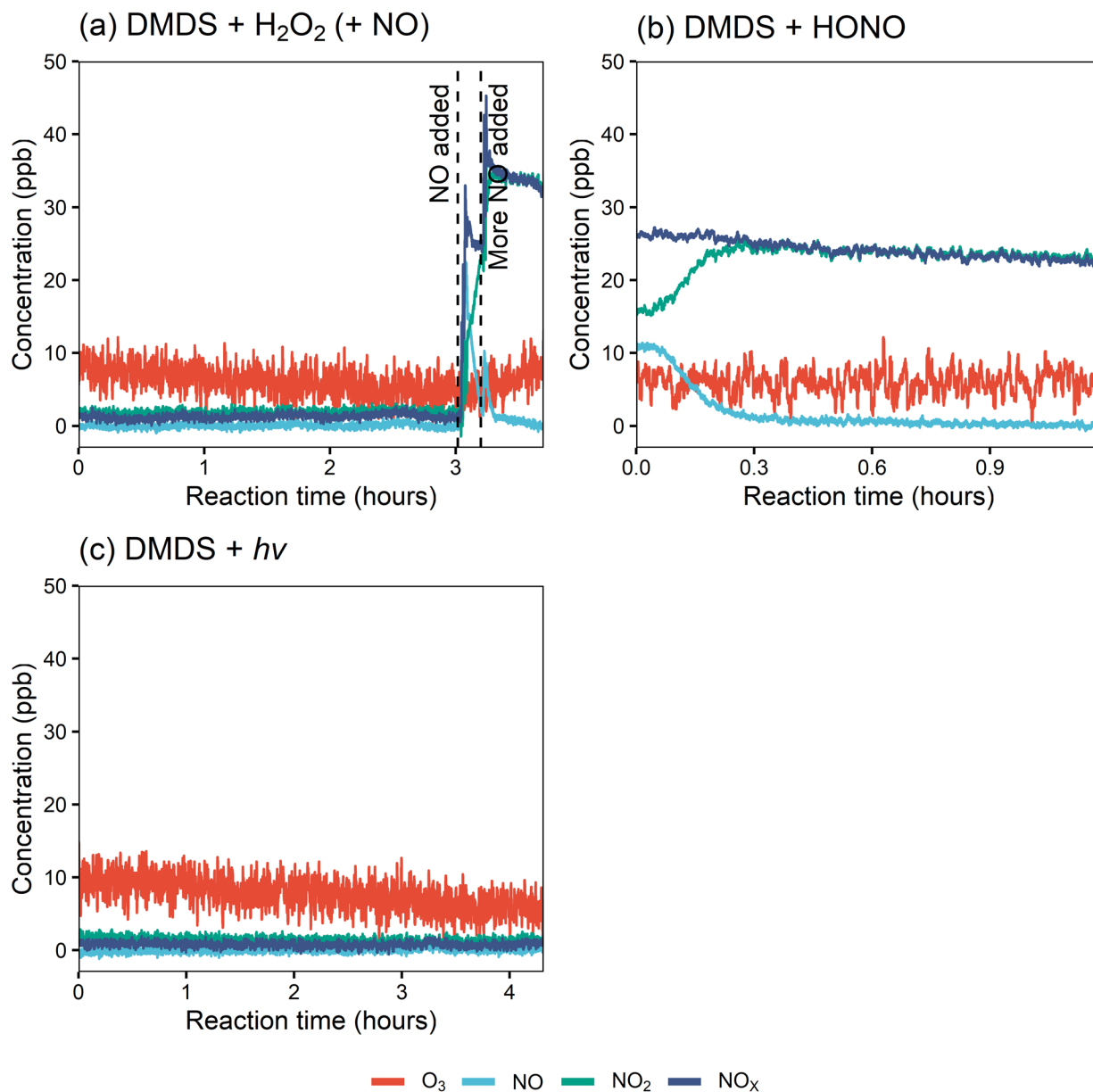
Figure S5: NO$_X$ and ozone timeseries from DMDS oxidation experiments (Panels a-c correspond to experiments 5-7 respectively). Note that NO$_Y$ species such as HONO are measured as NO$_2$ in the NO$_X$ monitor so "NO$_2$" represents NO$_2$ + NO$_Y$. No dilution corrections have been applied to these data. Note that the x-axes are different in each panel.

Figure S5 shows NO$_X$ and ozone timeseries from experiments in which DMDS was oxidized. Most notably, apparent ozone formation is considerably diminished compared to DMSO experiments, possibly due to several factors. The use of only 50% UV light intensity for experiments 5 and 6 should reduce the rate of NO$_2$ photolysis and therefore O$_3$ production by 50%. DMDS also interferes with the ozone measurement due to relatively strong absorption at the same wavelength used by the ozone monitor. This cross sensitivity is responsible for the nonzero O$_3$ concentrations at t = 0 in each experiment. Since detection of DMDS in the ozone

monitor requires that it be removed by the ozone scrubber in the instrument, its absorption on the scrubber may represent contamination that reduces the sensitivity of the instrument to ozone. The continued diffusion of HONO into the chamber that was seen for DMSO appears to have been negligible for experiment 6.

S.4 Total sulfur plots
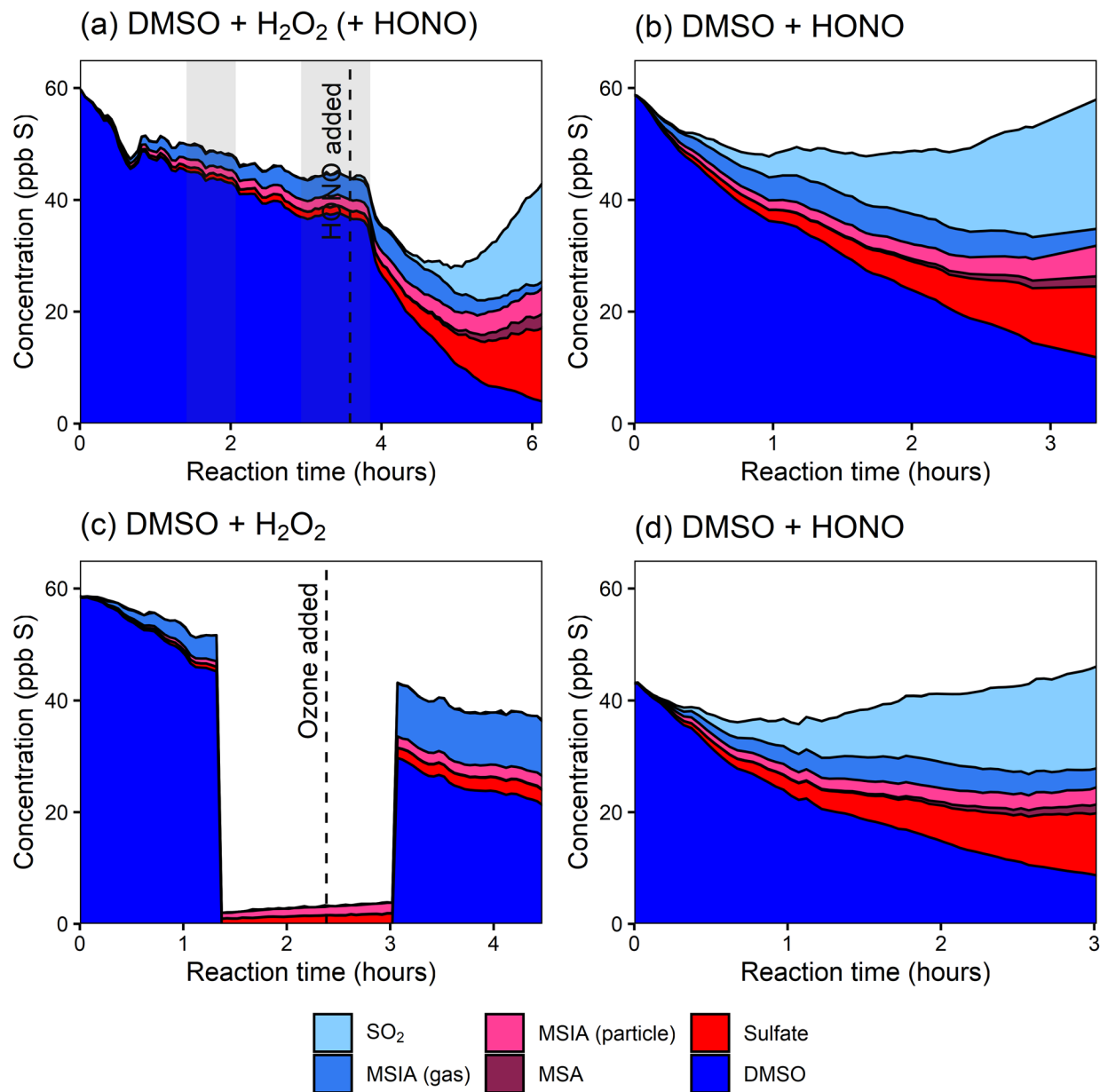
Figure S6: Stacked DMSO and product timeseries for the oxidation of DMSO with H₂O₂ (+ HONO addition) (experiment 1, Panel a), HONO (experiment 2, Panel b), H₂O₂ (experiment 3, Panel c), and HONO (experiment 4, Panel d) as OH precursors. The DMSO signal is somewhat unstable (esp. in experiment 1), likely representing a substantial contribution to the uncertainty. Sulfur closure is variable but suggests that most products are measured within uncertainty. Gray bars denote time periods when the lights were turned off for diagnostic purposes.
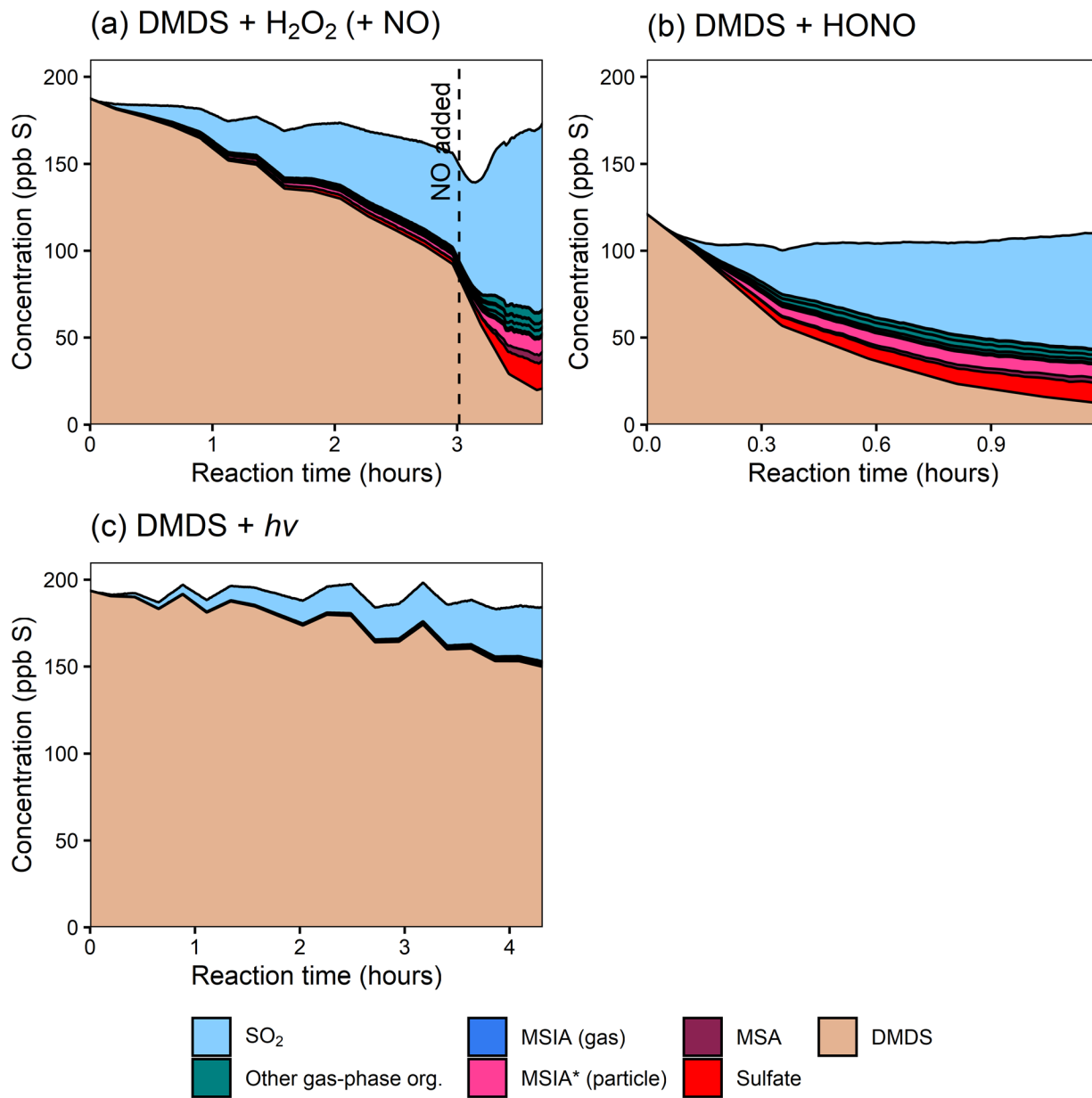
Figure S7: Stacked DMDS and product timeseries for the oxidation of DMDS with H₂O₂ (+ NO addition) (experiment 5, Panel a), and HONO (experiment 6, Panel b) as OH precursors, and the photolysis of DMDS (experiment 7, Panel c). Note that DMDS measurements are taken via GC-FID only every 13.75 minutes. The total sulfur measured remains relatively constant throughout each experiment, suggesting that no major products are unmeasured.

S.5 Product stack plots for additional experiments
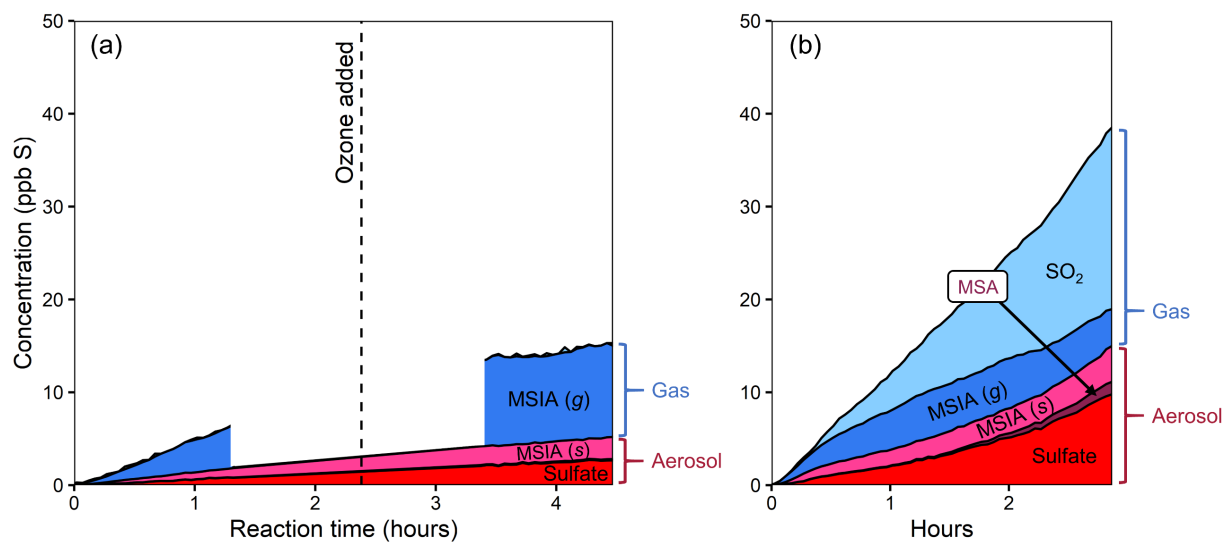
Figure S8: Stacked product timeseries from the oxidation of DMSO with H₂O₂ (experiment 3, Panel a) and HONO (experiment 4, Panel b) as oxidant precursors. The gap in the MSIA (g) timeseries for Panel a is due to a malfunction in dilution system in front of the NH₄⁺-CIMS inlet.
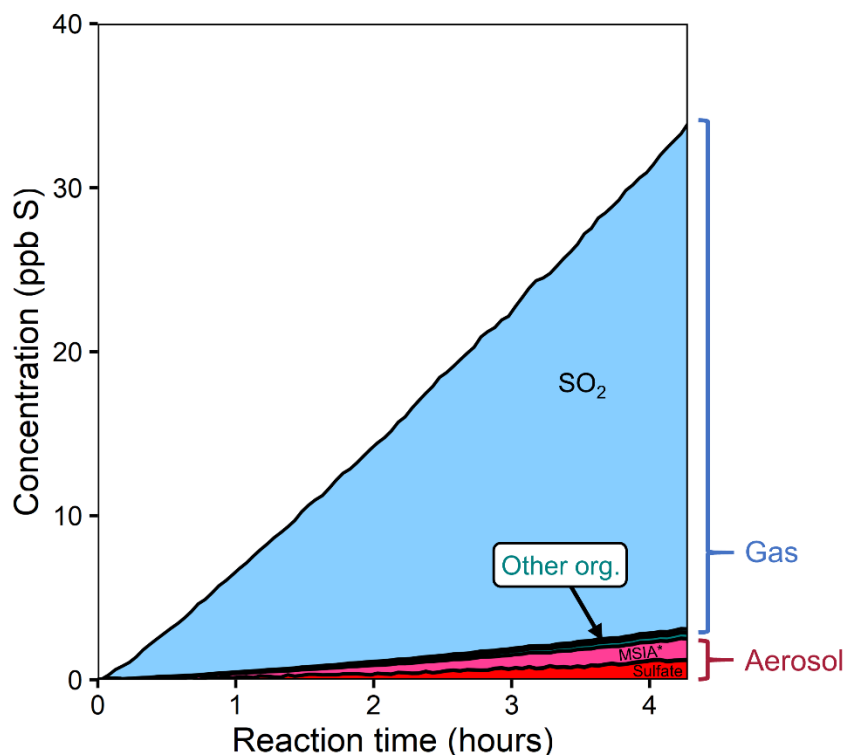
Figure S9: Stacked product timeseries from the photolysis of DMDS with no added oxidant precursor (experiment 7). All gas-phase organic compounds detected by the NH$_4^+$-CIMS except for MSIA (g) are shown in green as "Other org." and shown in greater detail in Fig. S13. Particle phase MSIA is marked with an asterisk to denote uncertainty in its exact chemical speciation.

S.6 Precursor signal smoothing

For both DMSO and DMDS, the precursor timeseries exhibit moderate noise for some experiments. Where this noise is substantial, non-monotonic decreases in the raw precursor signal would result in discontinuous yield curves (Figs. 3 and 6) when plotted using the "precursor lost" as an x-axis. To render the yield plots more easily interpretable, precursor timeseries are smoothed using penalized splines before a "precursor lost" vector is generated. These smoothed timeseries are shown in Figs. S10 and S11. The DMSO signal (C$_2$H$_6$SO(NH$_4^+$)) was less stable than the signals of other ions detected by the NH$_4^+$-CIMS, particularly for experiment 1 (Fig. S10a), suggesting that the DMSO concentration in the chamber may be somewhat uncertain.
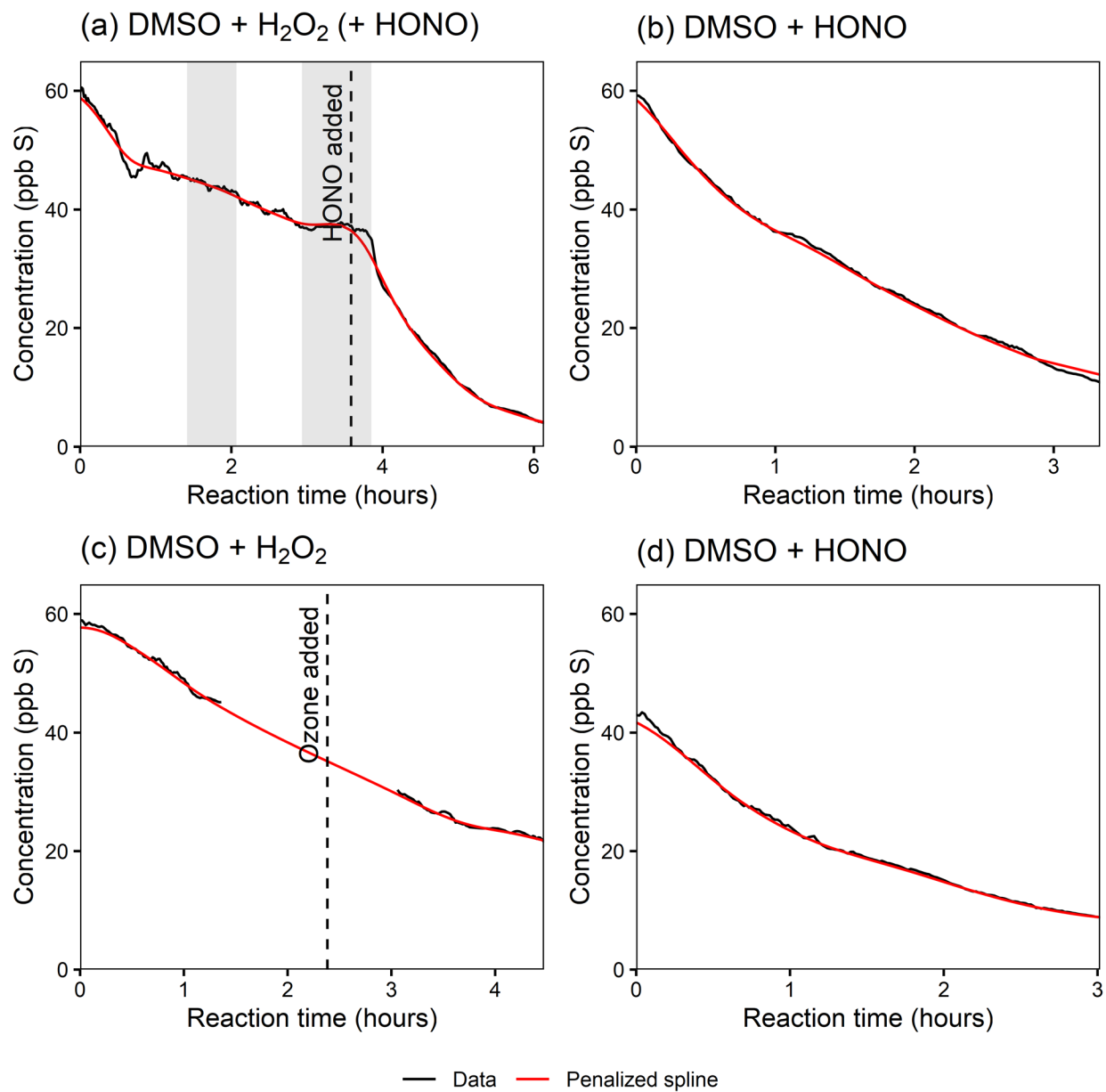
Figure S10: DMSO signal and penalized spline fits used for x-axes of the yield plots (Fig. 3). Panels a-d show data from experiments 1-4 respectively. The splines are fit using the "sm.spline" function from the "pspline" package in R, with spar values set to 1 x 10⁹. Gray bars denote times when the lights were turned off for diagnostic purposes.
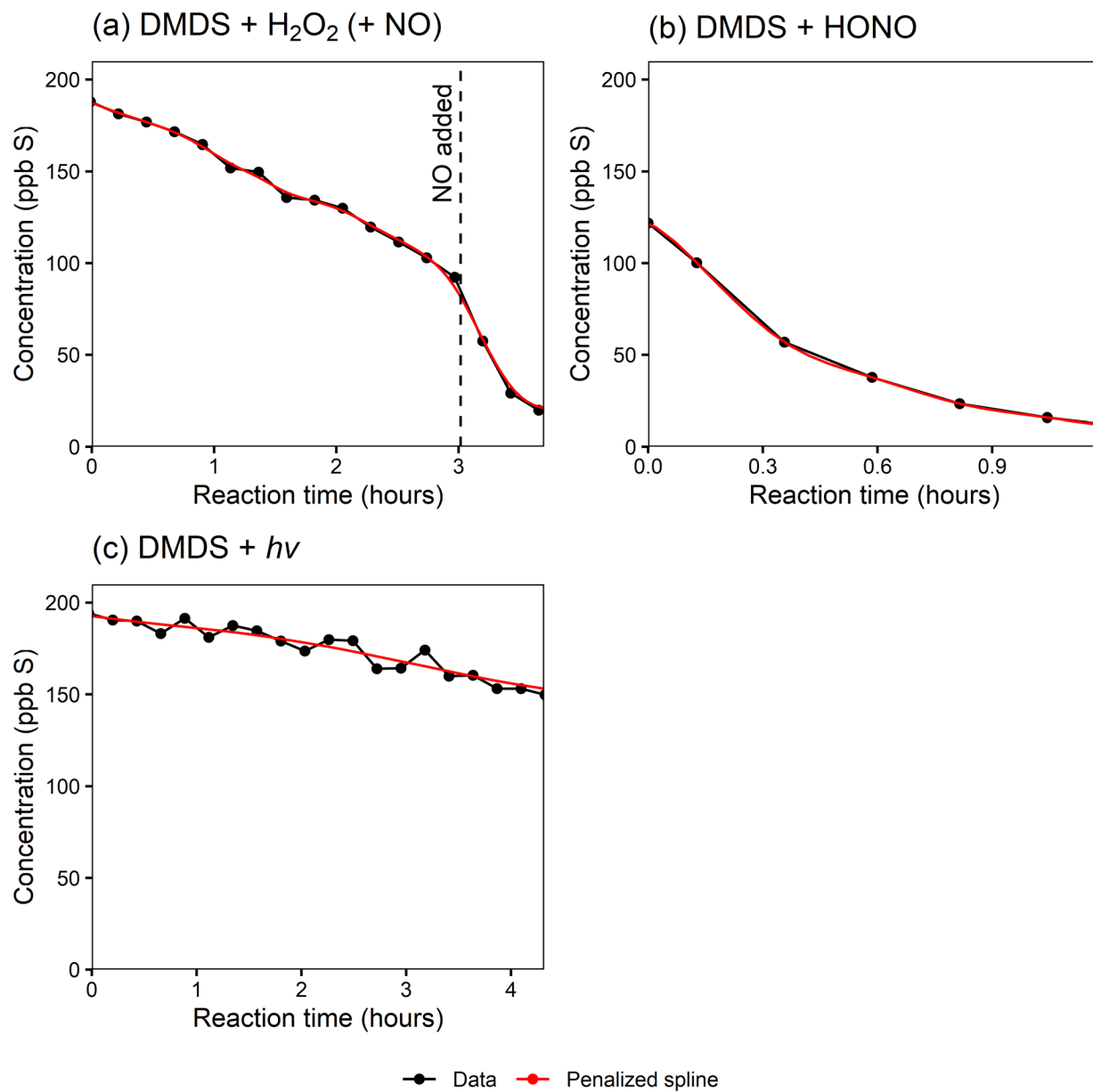
Figure S11: DMDS signal and penalized spline fits used for x-axes of the yield plots (Fig. 6). Panels a-c show data from experiments 5-7 respectively. The splines are fit using the "sm.spline" function from the "pspline" package in R, with spar values set to 1 x 10⁸, 1 x 10⁴, and 1 x 10¹⁰ respectively. The point at t = 0 for experiment 6 is extrapolated based on the three points before t = 0.

S.7 Additional yield plots
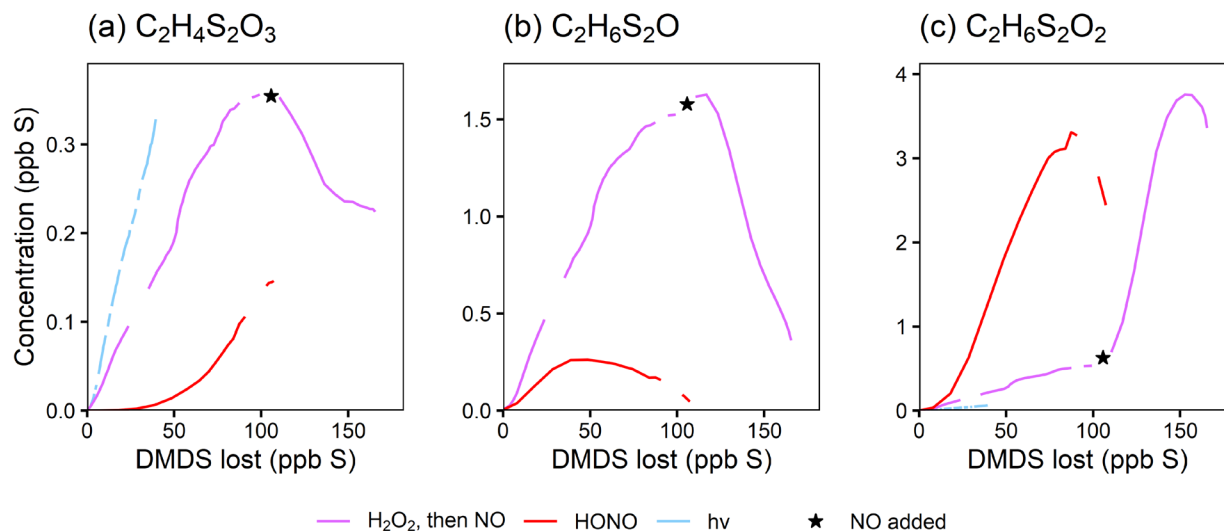
Figure S12: Additional yield plots for selected DMDS oxidation products. $C_2H_4S_2O_3$, $C_2H_6S_2O$, and $C_2H_6S_2O_2$ are plotted vs the loss of DMDS to normalize for changing OH concentrations, allowing comparisons between experiments 5-7. Colors denote experimental conditions. Note that for one experiment, the NO_X regime is switched by adding NO, as marked by the star. Note the differing y axes.

Figure S12 shows yield plots for $C_2H_4S_2O_3$, $C_2H_6S_2O$, and $C_2H_6S_2O_2$. The $C_2H_4S_2O_3$ signal is attributed to the isomerization product $HOOCH_2SSCHO$ (Fig. 1; Fig. S12a). This product is thought to be formed through abstraction of a methyl hydrogen from DMDS, followed by two isomerization steps, and is analogous to the formation of HPMTF from DMS (Berndt et al., 2020). The yield of this product shifts with experimental conditions in response to the RO_2 bimolecular lifetime. Photolysis conditions generate $C_2H_4S_2O_3$ in the highest yield, indicating that some OH is likely present and that alternative RO_2 sinks (HO_2 and NO) are quite low. Experiments using H_2O_2 and HONO as OH precursors (expts 5 and 6) involve shorter bimolecular lifetimes and lower $C_2H_4S_2O_3$ yields. Figures S12b and S12c are discussed in the following section.

S.8 Further discussion of NH4+-CIMS data
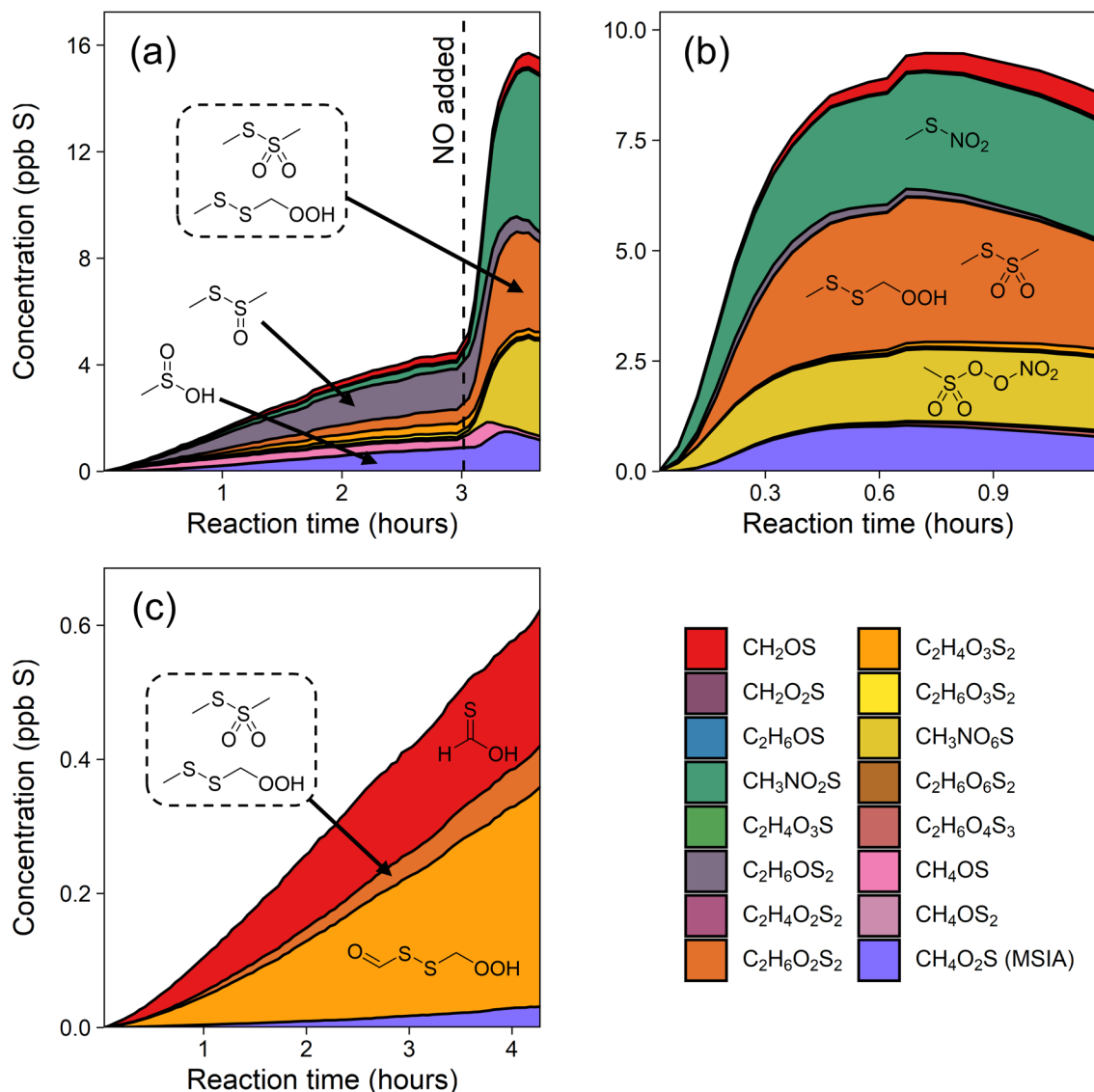
Figure S13: Stacked timeseries of minor gas-phase organosulfur products detected by the NH₄⁺-CIMS for experiments 5-7 (Panels a-c respectively). Hypothesized structures for the most abundant products are given. The legend lists the formulas for all closed-shell species detected in the NH₄⁺-CIMS. Note that the y-axis is different in each plot. Note that these plots include MSIA which is detected in the NH₄⁺-CIMS but not included in "Other org." as shown in Figs. 5 and 7 in the main text.
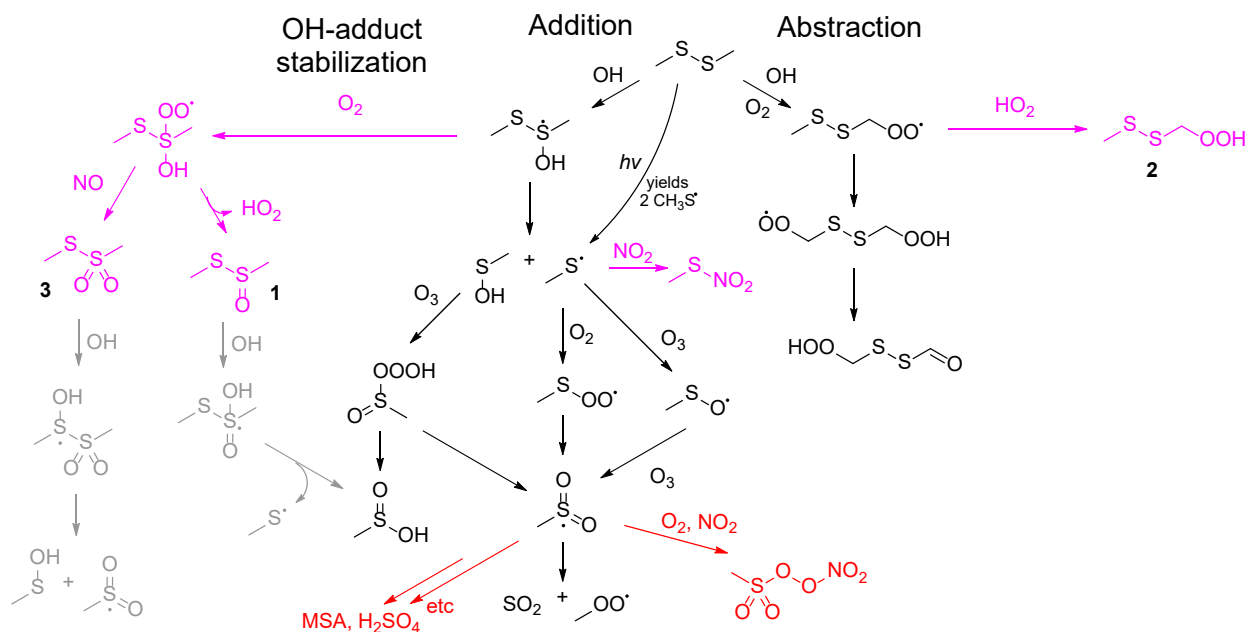
Figure S14: Detailed DMDS oxidation chemistry. Reactions shown in black are taken from Berndt et al. (2020). Reactions shown in red explain observed products based on known DMS chemistry (Saunders et al., 2003). Reactions shown in pink represent new hypothesized reaction pathways. Reactions in gray represent hypothesized secondary chemistry. Several compounds are numbered for reference in the text.

Figures S13 shows the timeseries of all gas-phase organics detected by the NH_4^+-CIMS and Figure S14 shows a detailed DMDS mechanism, based on these results. As discussed in the main text, $C_2H_6S_2O$ forms in greater yield under low NO conditions and is best explained by the structure $CH_3SS(O)CH_3$ (product **1** in Fig. S14; see also Fig. S12b). In contrast, $C_2H_6S_2O_2$ forms in greater yield under high NO conditions (Fig. S12c). This signal may be from CH_3SSCH_2OOH (product **2** in Fig. S14) at low [NO], but it is better explained by $CH_3SS(O)_2CH_3$ under high NO conditions (product **3** in Fig. S14). Additional oxidation via OH may lead to fragmentation (shown in gray in Fig. S14), resulting in the formation of established DMDS products.

S.9 Application of the new AMS quantification method to DMS-derived aerosol
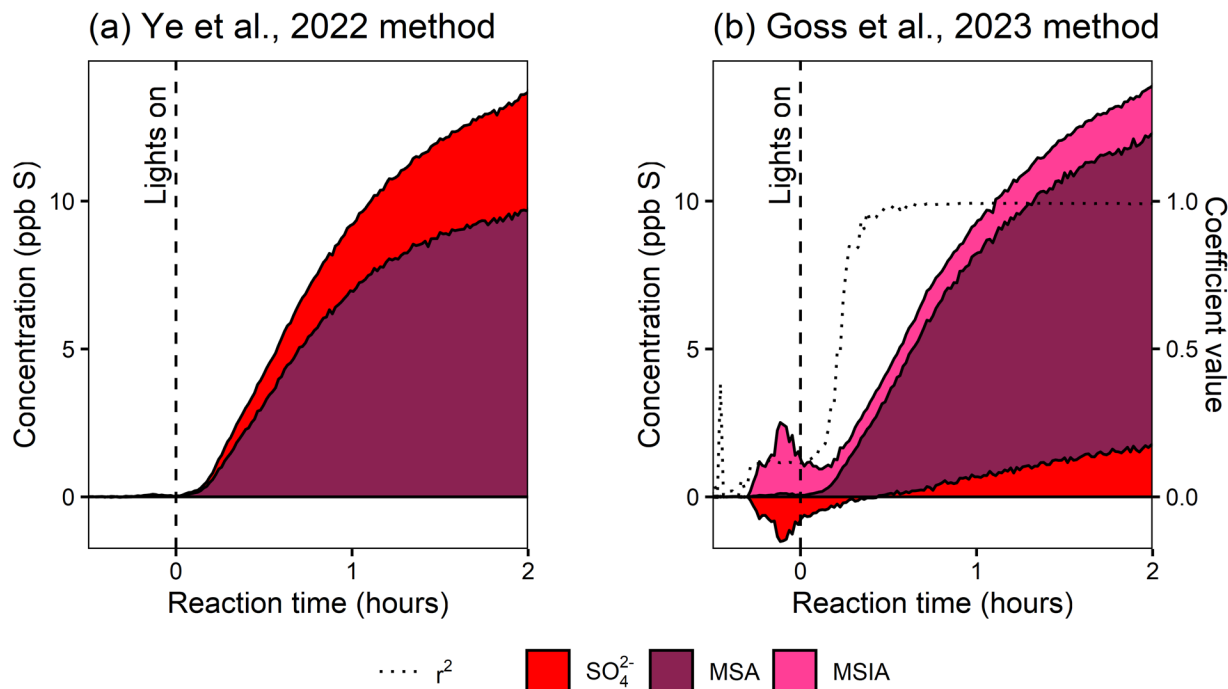
Figure S15: The results of two methods of AMS quantification applied to data from Ye et al., 2022, where DMS was oxidized by OH in the same chamber using HONO as an oxidant precursor. Panel a shows the product distribution using the method from Ye et al., 2022. This approach uses modifications to the frag table, based on Huang et al. (2017). Panel b shows the product distribution using the methods described in this paper (see section S.2). Panel b also shows the r^2 value from the derivation of MSA and MSIA timeseries using a linear combination. Note that RIE values, collection efficiency, wall loss, and dilution loss corrections have been applied as described in Ye et al., 2022.

As a test case, the AMS quantification method described above is applied to data from Ye et al. (2022). Figure S15 shows the results of the method from Ye et al. (2022) (Panel a), and from this work (Panel b) for an experiment in which dimethyl sulfide was oxidized using HONO as an oxidant precursor. For simplicity, the reference sulfate, MSA, and MSIA spectra used to generate the data shown in Panel b are those taken for this current work, likely adding uncertainty to this quantification.

The calculated aerosol product distribution is similar, but the new method favors MSA as an even more dominant product. In the method used in Ye et al. (2022), the SQUIRREL frag table is modified to apportion signal to MSA based on the signal at m/z 79. The remaining sulfate peaks are assigned to a sulfate timeseries, giving an MSA : sulfate ratio of ~2.4 : 1. When the new method is applied (Panel b), the spectrum from the seed aerosol (present in the chamber before t = 0) is explained by the linear fit to MSIA and MSA with a low but nonzero r^2 value. This results in a positive concentration of MSIA when none is present. The subtraction of MSIA from the residual spectrum results in a negative sulfate concentration. When the r^2 value

approaches 1 (Panel b), the calculated sulfate concentration is no longer negative. Under this method, the MSA : sulfate ratio increases to ~6.0 : 1 at the end of the experiment.

These results suggest that MSIA may be a minor but notable additional contributor to rapidly formed DMS-derived aerosol. The partitioning between gas- and particle-phase MSIA observed for this experiment (35 ± 8 % particle-phase (± 1 std. dev.)) agrees closely with that observed for DMSO products, giving additional confidence in the MSIA measurement. While the presented data show negative sulfate concentrations for the first few minutes of the experiment, it is likely that the use of contemporary reference spectra or a filter based on r^2 could address this. The use of this method could prove useful for future chamber or field measurements where MSA and MSIA are expected to dominate the organosulfur components of the AMS spectrum.

References

Berndt, T., Chen, J., Møller, K. H., Hyttinen, N., Prisle, N. L., Tilgner, A., Hoffmann, E. H., Herrmann, H., and Kjaergaard, H. G.: SO$_2$ formation and peroxy radical isomerization in the atmospheric reaction of OH radicals with dimethyl disulfide, Chem. Commun., 56, 13634–13637, https://doi.org/10.1039/D0CC05783E, 2020.

Hodshire, A. L., Campuzano-Jost, P., Kodros, J. K., Croft, B., Nault, B. A., Schroder, J. C., Jimenez, J. L., and Pierce, J. R.: The potential role of methanesulfonic acid (MSA) in aerosol formation and growth and the associated radiative forcings, Atmos. Chem. Phys., 19, 3137–3160, https://doi.org/10.5194/acp-19-3137-2019, 2019.

Holzinger, R.: PTRwid: A new widget tool for processing PTR-TOF-MS data, Atmos. Meas. Tech., 8, 3903–3922, https://doi.org/10.5194/amt-8-3903-2015, 2015.

Huang, S., Poulain, L., van Pinxteren, D., van Pinxteren, M., Wu, Z., Herrmann, H., and Wiedensohler, A.: Latitudinal and Seasonal Distribution of Particulate MSA over the Atlantic using a Validated Quantification Method with HR-ToF-AMS, Environ. Sci. Technol., 51, 418–426, https://doi.org/10.1021/acs.est.6b03186, 2017.

Koss, A. R., Canagaratna, M. R., Zaytsev, A., Krechmer, J. E., Breitenlechner, M., Nihill, K. J., Lim, C. Y., Rowe, J. C., Roscioli, J. R., Keutsch, F. N., and Kroll, J. H.: Dimensionality-reduction techniques for complex mass spectrometric datasets: application to laboratory atmospheric organic oxidation experiments, Atmos. Chem. Phys., 20, 1021–1041, https://doi.org/10.5194/acp-20-1021-2020, 2020.

Saunders, S. M., Jenkin, M. E., Derwent, R. G., and Pilling, M. J.: Protocol for the development of the Master Chemical Mechanism, MCM v3 (Part A): tropospheric degradation of non-aromatic volatile organic compounds, Atmos. Chem. Phys., 3, 161–180, https://doi.org/10.5194/acp-3-161-2003, 2003.

Ye, Q., Goss, M. B., Krechmer, J. E., Majluf, F., Zaytsev, A., Li, Y., Roscioli, J. R., Canagaratna, M., Keutsch, F. N., Heald, C. L., and Kroll, J. H.: Product distribution, kinetics,

and aerosol formation from the OH oxidation of dimethyl sulfide under different RO$_2$ regimes, Atmos. Chem. Phys., 22, 16003–16015, https://doi.org/10.5194/acp-22-16003-2022, 2022.

Zaytsev, A., Breitenlechner, M., Koss, A. R., Lim, C. Y., Rowe, J. C., Kroll, J. H., and Keutsch, F. N.: Using collision-induced dissociation to constrain sensitivity of ammonia chemical ionization mass spectrometry (NH4+ CIMS) to oxygenated volatile organic compounds, Atmos. Meas. Tech., 12, 1861–1870, https://doi.org/10.5194/amt-12-1861-2019, 2019.